





RESEARCH ARTICLE | JANUARY 27 2025

Wave-breaking phenomena around a wedge-shaped bow

Jianhua Wang (王建华) ; Yuming Shao (邵聿明) ; Xinyi Li (李心怡); Tianyi Mao (毛天仪);
Decheng Wan (万德成)  



Physics of Fluids 37, 012124 (2025)

<https://doi.org/10.1063/5.0252354>



Articles You May Be Interested In

Numerical investigation of flow structure and air entrainment of breaking bow wave generated by a rectangular plate

Physics of Fluids (December 2021)

Experiments on the water entry of asymmetric wedges using particle image velocimetry

Physics of Fluids (February 2015)

Numerical simulation of the influence of wave parameters on the horizontal cylinder in the nonlinear coupling of the wave–current

Physics of Fluids (August 2024)



Physics of Fluids

Special Topics Open
for Submissions

[Learn More](#)

Wave-breaking phenomena around a wedge-shaped bow

Cite as: Phys. Fluids **37**, 012124 (2025); doi: [10.1063/5.0252354](https://doi.org/10.1063/5.0252354)

Submitted: 9 December 2024 · Accepted: 2 January 2025 ·

Published Online: 27 January 2025



View Online



Export Citation



CrossMark

Jianhua Wang (王建华), Yuming Shao (邵聿明), Xinyi Li (李心怡), Tianyi Mao (毛天仪), and Decheng Wan (万德成) ^{a)}

AFFILIATIONS

Computational Marine Hydrodynamics Lab (CMHL), School of Naval Architecture, Ocean and Civil Engineering, Shanghai Jiao Tong University, Shanghai 200240, China

^{a)} Author to whom correspondence should be addressed: dcwan@sjtu.edu.cn

ABSTRACT

Bow wave breaking has long been a research challenge in the research field of ship hydrodynamic. This study simplifies the ship's bow as a three-dimensional wedge-shaped structure and conducts experimental measurements to investigate the dynamic characteristics of bow wave breaking. The experiments are carried out in a recirculating water channel, with the force transducer and wave height probes used for measurement. The complex mechanisms influencing bow wave breaking in real-world scenarios can be influenced by factors such as flow velocity, draft, flooding angle, flare angle, and yaw angle. Experiments are carried out under various conditions by controlling one factor at a time. The results show that more intense wave breaking not only increases the resistance force on the wedge but also raises the wave height of the measuring point in the non-breaking region and the nonlinearity in the breaking region. The high-frequency fluctuations of wave height in the breaking region become more obvious. Through a quantitative comparison of different factors on the wave-breaking phenomena, it can be found that the flooding angle has a significant impact on resistance, which helps explain why slender hull designs are commonly used for fast ships. The yaw angle plays a crucial role in affecting the bow waves, influencing both stable wave height and nonlinear breaking waves. The measurement results presented in this paper can provide valuable validation data and flow insights for studies on ship bow wave breaking.

Published under an exclusive license by AIP Publishing. <https://doi.org/10.1063/5.0252354>

I. INTRODUCTION

The phenomenon of bow wave breaking is crucial in the fields of ship and ocean engineering for several reasons:^{1,2} (1) Bow wave breaking inevitably generates wave-breaking resistance, leading to additional fuel consumption. (2) As the bow wave curls and interacts with the free surface, air bubbles are entrained, creating a trail of white foam on the water surface, which poses a threat to the stealth capabilities of naval vessels. (3) The downward sweep of bubbles at the bow can interfere with underwater sonar equipment. (4) Severe wave-breaking can also impact nearby structures, such as ferries and breakwaters, especially in restricted water. The breaking waves are also accompanied by water droplets and bubbles, which are small in size but play an important role in energy transfer.³ Moreover, the trend toward green, low-carbon, energy-efficient shipping is a global priority for the future of the marine industry. Conducting in-depth research on ship bow wave breaking offers new perspectives and methodologies for improving ship hydrodynamic performance prediction, providing a necessary theoretical foundation and technical support for the optimal design of eco-friendly ships.

Currently, research on bow wave breaking is typically conducted through model tests, where researchers observe and measure the physical flow phenomena involved. Numerous studies have examined the changes in bow wave patterns at different speeds.⁴⁻⁷ High-speed photography has been used to capture the morphology of wave breaking and the location of separation points, revealing the evolution and distribution characteristics of bow wave breaking with varying speeds. Olivieri *et al.*⁸ conducted model tests on the DTMB 5415 standard ship, capturing images of wave breaking under various conditions and recording wave height variations using scales. Additionally, PIV (Particle Image Velocimetry) equipment was used to measure the velocity distribution at different sections, attempting to provide quantitative experimental results of bow wave breaking. Drazen *et al.*⁹ studied stern wave breaking in a flat-stern vessel at Froude numbers between 0.27 and 0.5. Using laser sensors, they measured the average height and root mean square values of breaking waves in the wake at different speeds, and high-resolution flow field data were used to quantify wave height distribution. Choi *et al.*¹⁰ used high-speed cameras to

experimentally study bow wave breaking in two ship types—a slender ship and a fuller ship—observing both curling and spilling wave-breaking phenomena. Liu *et al.*¹¹ carried out model tests on bow wave breaking under different trim conditions using the KCS standard ship, measuring waveforms and concluding that bow wave breaking is more intense under the nose-down condition.

In recent years, with the development of computational fluid dynamics (CFD), more scholars have used numerical simulation to study bow wave breaking.^{12–14} Hendrickson *et al.*^{15,16} employed a Cartesian grid method combined with Direct Numerical Simulation (DNS) or Large Eddy Simulation (LES) to provide fine-grained predictions of stern wave breaking in flat-stern vessels. Their simulations used the conservative Volume of Fluid (VOF) method and an immersed boundary method to model the hull boundary, capturing detailed features such as wave curling and air entrainment. Their results demonstrated that high-precision wave-breaking simulations can be achieved using interface-resolving techniques, though this method is currently applicable only to simple geometries and comes at a high computational cost. Wang *et al.*^{17–19} used an OpenFOAM-based hydrodynamic CFD solver, employing an algebraic VOF method with an artificial compression term to simulate bow wave breaking in KCS and DTMB ships at high speeds. Their simulations used overlapping grids to refine the bow wave region, providing numerical predictions of bow wave breaking with lower computational costs. However, their method struggled to accurately capture details such as splashing and bubble entrainment. Although some researchers have done very detailed simulation of breaking waves with high-resolution results of water droplets and air entrainments,^{20–22} it is still very hard to have a better simulation result of breaking waves with marine structures.

These studies have shed light on the mechanisms of bow wave breaking in specific ship models. However, much of the current research focuses on standard ship models like KCS and DTMB with complex surfaces, investigating factors such as speed and trim angle. The factors affecting bow wave breaking are diverse and comprehensive. How to clearly reveal the influence of various factors on bow wave breaking remains a topic of interest. Waniewski *et al.*²³ simplified the bow to a wedge-shaped structure and conducted towing experiments in both flume and towing tanks, noting that bow waves are highly nonlinear and lack a theoretical solution. They observed surface disturbances caused by gravity waves, which were identified as the main reason for jet breakup into droplets and the formation of periodic bubble clouds.^{24,25} Karion *et al.*²⁶ further studied wedge-shaped bow wave breaking with two different entrance angles in a deep water towing basin. They found that wave breaking occurs when both Froude and Reynolds numbers exceed critical values, while spray formation is related to the Weber number. Noblesse *et al.*²⁷ replaced the wedge-shaped bow of a ship with a flat plate and conducted experiments in a towing tank at the École Centrale de Nantes, France, under various conditions. They provided theoretical prediction formulas for key wave characteristics (wave height, wave peak position, wave climbing, and wave profile) based on bow characteristics (speed, draft, and waterline entrance angle). These studies suggest that simplifying the bow into a wedge-shaped structure allows for better analysis of the various factors influencing bow wave breaking. However, the previous study still lacks of the experimental data of how the parameters, such as the bow shape geometry, influencing bow wave breaking.

In the present paper, the wedge-shaped structure with various geometries is used to investigate bow wave-breaking phenomena. The main objective of the present study is to find the effects of different factors, i.e., flow velocity, draft, flooding angle, yaw angle, and flare angle on bow wave breaking. This paper is structured as follows: the experimental approach including the platform, setup, test conditions, and data processing methods is introduced in Sec. II. Section III discusses the influence of various factors on breaking bow waves and their comparisons. Finally, Sec. IV provides a summary of the findings.

II. EXPERIMENTAL APPROACH

A. Experimental platform

The experiments are conducted in the wind-wave-current flume at Shanghai Jiao Tong University. This flume features a vertical loop structure, as shown in Fig. 1(a), and consists of three main sections: the test section, the guide vane section, and the power section.²⁸ It is capable of simulating complex marine environments, including wind, waves, and currents. The test section is 8.0 m long, 3.0 m wide, and 1.95 m deep, with a maximum flow velocity of 3.0 m/s. To mitigate the effects of boundary layer velocity deficits, a surface flow accelerator is installed upstream of the test section, ensuring flow field non-uniformity remains below 1.5%. Additionally, the facility is equipped with an automatic water filtration system and an automated water level control system.

B. Experimental setup

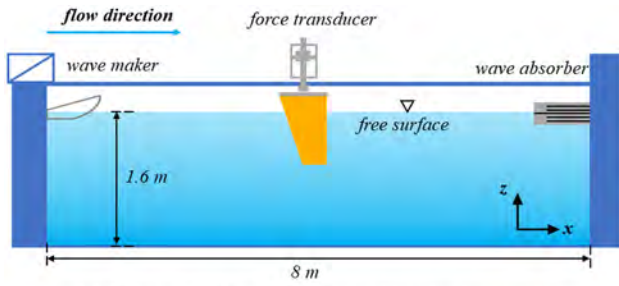
The experimental setup is illustrated in Fig. 2. A wedge-shaped body is fixed at the center of the circulating tank. The top of the wedge is connected to a force transducer via a steel plate to monitor the resistance force acting on the wedge under incoming flow conditions. As shown in Fig. 2(b), two wave height probes are positioned on the left side of the wedge to measure the time history of wave height data. The water temperature is 32 °C during the experiment.

C. Experimental condition

The experimental model is shown in Fig. 3, where the test model is a wedge-shaped structure with an isosceles triangular cross section in the XY plane. The chord length of the top panel of the wedge is



FIG. 1. Test section of the experimental facility at SJTU.



(a) Schematic diagram of experiment arrangement



Wave height probe
(b) Actual experiment arrangement

FIG. 2. Experimental setup at circulating tank.

$L = 0.75$ m, the total height is $H = 0.5$ m, and the draft is d . The model has three variable parameters: flooding angle θ , yaw angle γ , and flare angle α . The flooding angle refers to the angle between the longitudinal plane of the wedge and its top panel edge. The yaw angle represents the angle between the longitudinal plane of the wedge and the incoming flow direction. The flare angle is defined as the angle between the leading edge of the wedge and the horizontal plane. All these parameters are used to simplify the geometry of an actual ship's bow, with each parameter representing different shapes of the bow or varying conditions.

The parameters of the wedge are summarized in Table I. The longitudinal position of the wave height probes corresponds to their distance from the vertex of the top panel ($\Delta X = 0.9L \cos \theta$), while the transverse position represents the distance from the top panel's side-wall to the wave probes. To facilitate the observation of wave heights along the surface of the wedge, black-and-white grid paper with a grid size of 1 mm is affixed to its side.

D. Data processing method

The experimental data are obtained from the force transducer and wave height probes. The data primarily consist of time-history records for three channels, labeled as F_x , h_1 , and h_2 . These data correspond to the x-direction force measured by the force transducer and the wave height data from the two wave height probes, respectively. Since both the force transducer and wave height probes provide relative measurements, a zero-point calibration is performed for each test

condition under static water conditions. The zero-point calibration lasted 30 s, while the data collection period is 90 s, with a sampling interval of 0.02 s. For data averaging, the mean value of the 90-s dataset is first calculated. This mean is then corrected by subtracting the average value of the 30-s zero-point calibration data. Wave height data are filtered using a fourth-order Butterworth low-pass filter with a cutoff frequency of 0.5 Hz. This filtering process is applied to the wave height time-history data after subtracting the zero-point mean value.

To better represent the nonlinear effects of breaking waves, the root mean square (RMS) of the wave height is calculated to illustrate the breaking behavior. The mean value h_{mean} and RMS value h_{rms} can be computed using the following equations:

$$h_{mean} = \frac{\sum_{i=1}^n h_i}{n}, \tag{1}$$

$$h_{rms} = \sqrt{\frac{\sum_{i=1}^n (h_i - h_{mean})^2}{n}}, \tag{2}$$

where h_i stands for the i th record of wave height and n represents the time series has n values.

III. RESULTS AND DISCUSSION

A. Validation of experimental data

To validate the measurement data, all experiments were conducted with three repeated tests (designated as Test #1, Test #2, and Test #3). As an example, we present the test condition with a flow velocity of 2.5 m/s, a flooding angle of $\theta = 15^\circ$, a yaw angle of $\gamma = 0^\circ$, and a flare angle of $\alpha = 90^\circ$ to compare the results of the repeated tests. Figures 4–6 display the time histories of resistance and wave probe data at two locations from the three repeated tests. The results show good consistency in the measurement data for both resistance and wave height. However, the wave probe data at Point 4 exhibit greater oscillations due to the wave-breaking phenomenon in this region. To further assess the quality of the repeated test data, Tables II–IV provide a quantitative comparison of the measured resistance and wave height across the three repeated tests.

Table II shows the results of resistance and wave height from the three repeated tests, where F_{xi} , h_{1i} , and h_{2i} represent the i -th data of resistance, wave height of probe1 and probe2, respectively. Tables III and IV compare the results from the three repeated tests for resistance and wave height. The deviation is calculated by the error between two cases ($E = \frac{V_2 - V_1}{V_1}$). It can be observed that the deviation in resistance across different runs is up to 0.2%, while the deviation in wave height at the non-breaking area is less than 0.23%. However, in the breaking area, the wave height deviation is slightly larger, with errors reaching up to 2.51%. Overall, the measurement data from the three repeated tests show good consistency, and the experimental data can be considered reliable for studying the hydrodynamic performance of breaking waves around the wedge-shaped bow.

B. Draft effect

In the investigation of the draft effect, the flow velocity is kept constant at 2.5 m/s. The selected subject is a wedge with a flooding angle θ of 30° , a flare angle α of 90° , and a yaw angle γ of 0° . The drafts are set to $d = 0.05$ m, $d = 0.075$ m, and $d = 0.1$ m, respectively. In the experiment, we primarily focus on the resistance forces acting on the wedge and the wave heights at specific locations, as well as how

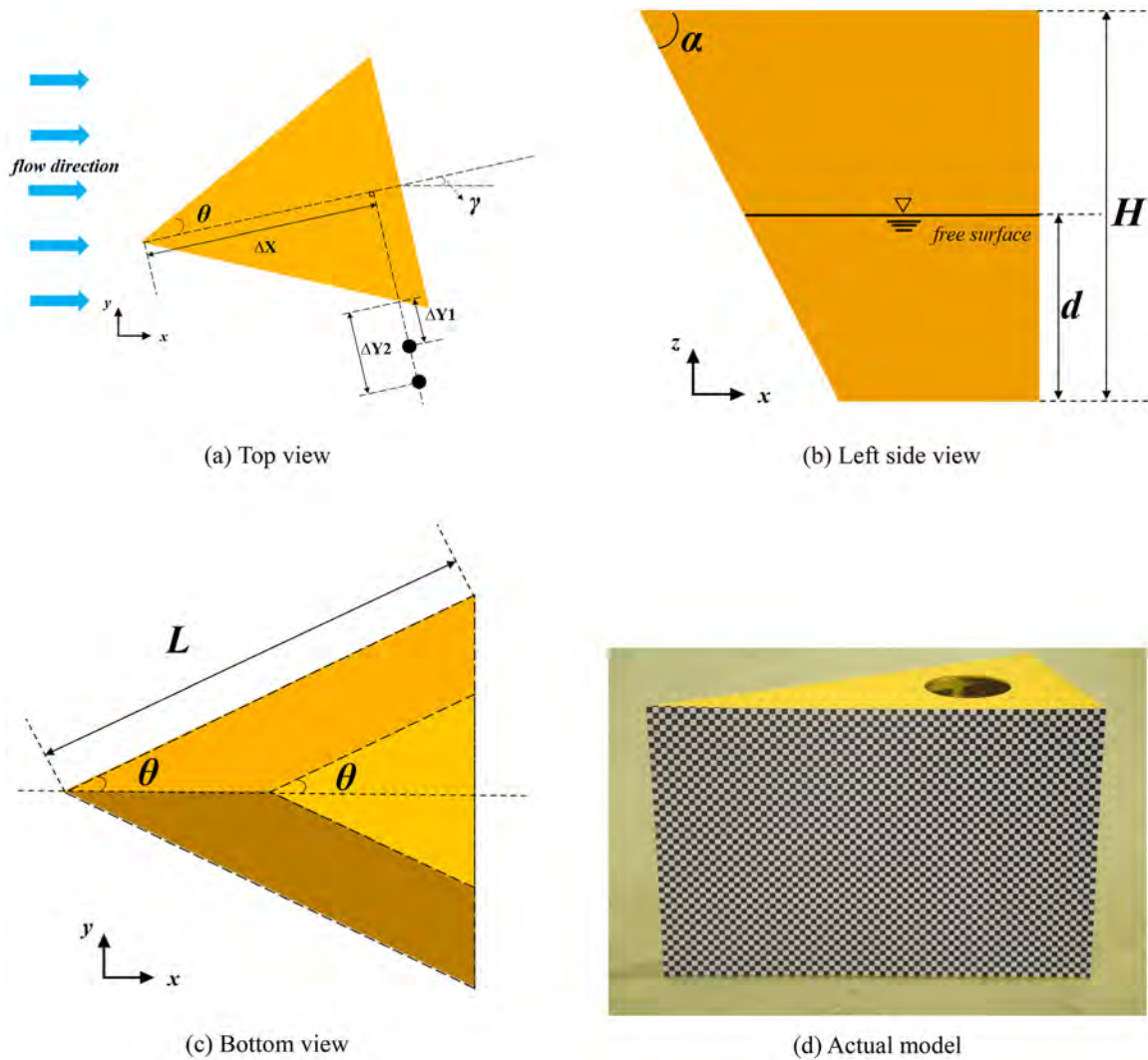


FIG. 3. Experimental model.

TABLE I. Main parameters of wedge and test conditions.

Parameters	Symbol	Value
Length	L (m)	0.75
Height	H (m)	0.5
Draft	d (m)	0.05, 0.075, 0.1
Flooding angle	θ ($^\circ$)	30, 22.5, 15
Yaw angle	γ ($^\circ$)	0, 5, 10, 15, 17.5, 20, 22.5
Flare angle	α ($^\circ$)	90, 80, 70
Flow velocity	U (m/s)	2, 2.5, 3
Longitudinal position of wave probes	ΔX (mm)	650, 693, 724
Transverse position of wave probes	ΔY (mm)	103, 205, 89, 425

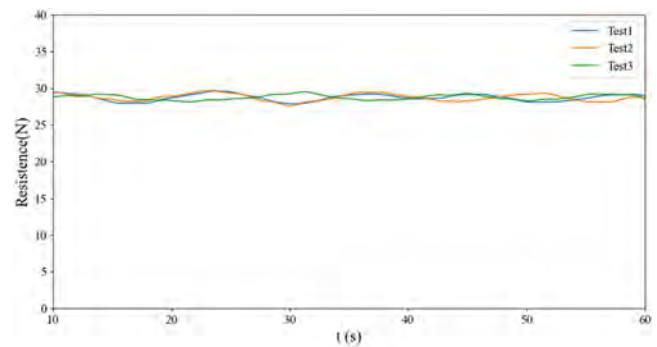


FIG. 4. Time histories of resistance from three repeated tests.

29 January 2025 15:21:08

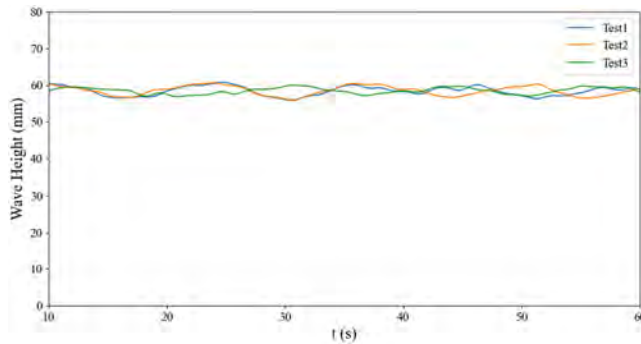


FIG. 5. Time histories of wave height h_1 from three repeated tests.

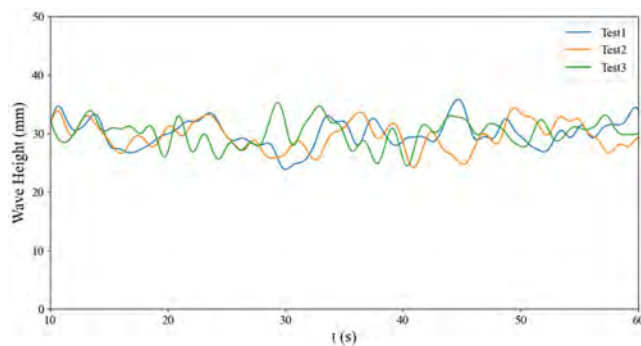


FIG. 6. Time histories of wave height h_2 from three repeated tests.

these wave heights changes over time. The wave probe in draft effect research is set at $\Delta Y_1 = 89$ mm and $\Delta Y_2 = 425$ mm, and the corresponding wave height is h_1 and h_2 . Three test perspectives—the front, side-rear, and side views—are displayed in Fig. 7 to better show how draft affects breaking waves. It can be observed that all three cases show similar breaking characteristics, where the plunging and overturning of bow waves are very violent. The plunging-type wave breaking creates a noticeable scar when the plunger interacts with the free surface, leading to significant air entrainment and bubble mixed flow.

The time-averaged resistance forces and wave heights for different drafts are recorded in Table V. It can be seen from the table that as the draft decreases, the resistance decreases rapidly. This is mainly due to the change of wet surface area. In addition, the wave heights at both locations show that as the draft increases, the wave height also increases. It indicates that the increase in draft enhances the intensity

TABLE II. Reproducibility of experiment data.

Experiment	Average longitudinal resistance (N)	Average wave heights at Probe1 (mm)	Average wave heights at Probe2 (mm)
Test #1	F_{x1} 28.697	h_{11} 58.316	h_{21} 29.762
Test #2	F_{x2} 28.714	h_{12} 58.352	h_{22} 29.409
Test #3	F_{x3} 28.755	h_{13} 58.452	h_{23} 30.167
Average	$\overline{F_x}$ 28.722	$\overline{h_1}$ 58.373	$\overline{h_2}$ 29.779

TABLE III. Deviation of resistance between three repeated tests.

Deviation	$E(\%)$
F_{x1} and F_{x2}	0.06
F_{x1} and F_{x3}	0.20
F_{x2} and F_{x3}	0.14

TABLE IV. Deviation of wave heights between three repeated tests.

Wave height deviation of Probe1		Wave height deviation of Probe2	
h_{1i} and h_{1j}	$E(\%)$	h_{2i} and h_{2j}	$E(\%)$
h_{11} and h_{12}	0.06	h_{21} and h_{22}	1.2
h_{11} and h_{13}	0.23	h_{21} and h_{23}	1.34
h_{12} and h_{13}	0.17	h_{22} and h_{23}	2.51

of the bow waves around wedge. This is consistent with the previous findings.²⁷

To study the temporal variation of wave height, wave height curves for different drafts are plotted as shown in Fig. 8. It can be observed that for h_1 , located in the stable region of the bow wave, the wave heights exhibit a clear periodicity at different drafts. For h_2 , located in the breaking region of the bow wave, the periodicity of wave heights becomes less distinct, and the high-frequency fluctuations significantly increase. For h_2 , the RMS of wave heights increases with the draft, indicating that jet formation and droplet splashing vary across different cases, which, in turn, affects the breaking intensity and high-frequency characteristics.

C. Flooding angle effect

In this section, three wedges with different flooding angles are used to study the effect on bow wave breaking. Flooding angles are set to $\theta = 15^\circ$, $\theta = 22.5^\circ$, and $\theta = 30^\circ$. In addition to the flooding angles, the flare angle α and yaw angle γ for all three models are set at 90° and 0° , respectively. The flow velocity is kept constant at 2.5 m/s, and the draft is set to $d = 0.075$ m. The wave probe is set at $\Delta Y_1 = 89$ mm, $\Delta Y_2 = 425$ mm, and the corresponding wave height is W_1 , W_2 , when $\theta = 22.5^\circ$ and $\theta = 30^\circ$. The wave probe is set at $\Delta Y_1 = 103$ mm, $\Delta Y_2 = 205$ mm, and the corresponding wave height is h_1 , h_2 , when $\theta = 15^\circ$. The experimental images are shown in Fig. 9.

As observed in Fig. 9, an increase in the flooding angle leads to a significant rise in both the extent of wave breaking and its intensity. A larger flooding angle amplifies the blockage effect of the inflow, which enhances wave run-up and results in more severe plunging waves.

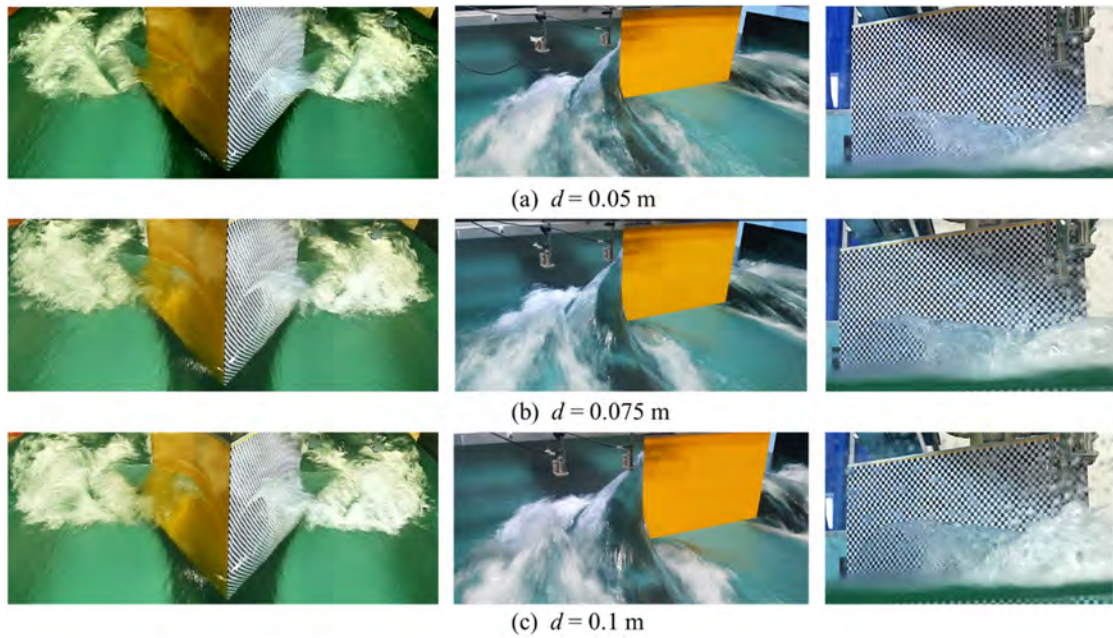


FIG. 7. Experimental images of bow waves at different drafts.

TABLE V. Resistance forces and wave heights at different drafts.

d (m)	F_x (N)	h_1 (mm)	h_2 (mm)	h_{2rms}
0.1	165.306	141.318	134.130	14.855
0.075	120.063	126.696	129.903	11.035
0.05	77.627	108.258	99.176	6.120

Consequently, wave overturning and subsequent wave splashing become more pronounced. This increased wave run-up directly contributes to a significant rise in resistance forces. From Table VI, it can be seen that as the flooding angle increases, the wave height at the same location also increases. This can be attributed to the reduction in the range of bow waves caused by a decrease in the flooding angle. It should be noticed that the wave height for a flooding angle of $\theta = 15^\circ$ is at different locations due to the bow wave region differs a lot with the other cases. However, the wave height remains lower than for

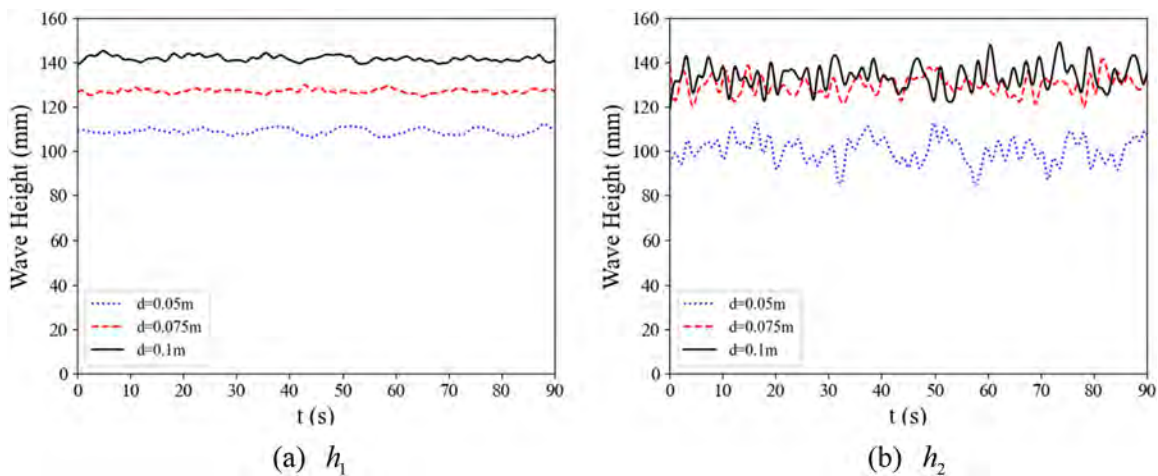


FIG. 8. Time histories of wave height at different drafts.

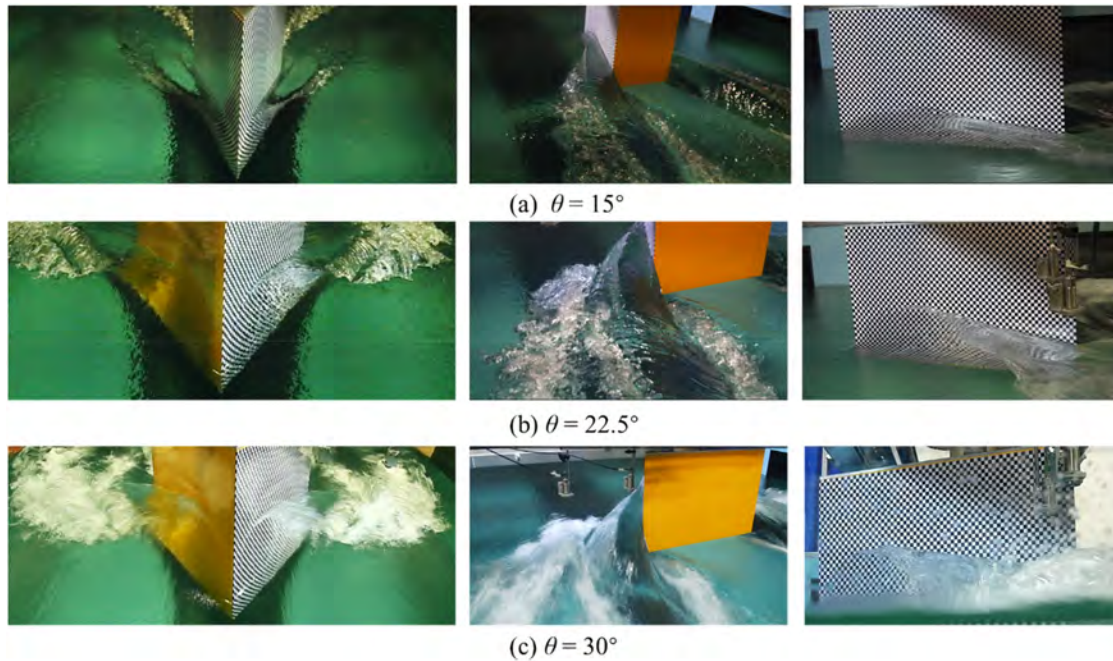


FIG. 9. Experimental images of bow waves at different flooding angles.

larger angles, further supporting the conclusion that the bow wave range decreases with a smaller flooding angle.

Wave height curves for different flooding angles are shown in Fig. 10. It can be observed that as the flooding angle increases, the mean wave height in the stable bow wave region also increases. In the wave-breaking region, high-frequency fluctuations are clearly evident in all three cases, which explains the nonlinear behavior of the breaking waves. The RMS values listed in Table VI further reflect these high-frequency characteristics, with h_{2rms} being much smaller in the case of a smaller flooding angle. This observation is consistent with the flow images shown in Fig. 9.

D. Flare angle effect

To study the effect of different flare angles, the selected subject is a wedge with a flooding angle θ of 30° and a yaw angle γ of 0° . The flow velocity is set to $U = 0.25 \text{ m/s}$, and the draft is set to $d = 0.075 \text{ m}$. The test chooses three different flare angles, which are $\alpha = 70^\circ$, $\alpha = 80^\circ$, and $\alpha = 90^\circ$. The wave probe is set at $\Delta Y_1 = 103 \text{ mm}$, $\Delta Y_2 = 205 \text{ mm}$, and the corresponding wave height is h_1, h_2 .

Figure 11 displays photographs taken from three experiments at different flare angle conditions, and Table VII provides the

corresponding resistance force and wave height data. From the figures, it can be observed that smaller flare angles lead to lower bow wave heights and a more restricted wave breaking and overturning region. As a result, the resistance force decreases by up to 61.9%. Since the draft is very small, and the wetted surface area is relatively limited, the reduction in resistance is primarily attributed to a decrease in wave-making resistance. This finding helps explain why high-speed vessels often incorporate flared bow designs.

Additionally, the wave height measurements h_1 and h_2 are very similar for flare angles $\alpha = 70^\circ$ and $\alpha = 80^\circ$, indicating that in these conditions, the wave-breaking region does not extend to the positions of the wave height probes. It can also explain why the RMS value very small in these two cases. In contrast, for $\alpha = 90^\circ$, the wave breaking covers a significantly larger area. This suggests that within the range $80^\circ \leq \alpha \leq 90^\circ$, the degree of bow wave breaking undergoes substantial changes. Figure 12 presents the time histories of wave heights for the three flare angle conditions. Similar to Fig. 8, the non-breaking wave regions exhibit a clear periodic pattern. In contrast, the curves in the wave-breaking regions display significant high-frequency fluctuations due to the nonlinear phenomena of small-scale flow features.

E. Flow velocity effect

The selected model is a wedge with a flooding angle θ of 30° , a flare angle α of 90° , a yaw angle γ of 0° , and a draft d of 0.075 m . The conditions of flow velocity are set to $U = 0.20 \text{ m/s}$, $U = 0.25 \text{ m/s}$, and $U = 0.30 \text{ m/s}$. The wave probe is set at $\Delta Y_1 = 89 \text{ mm}$, $\Delta Y_2 = 425 \text{ mm}$, and the corresponding wave height is h_1, h_2 .

Experimental images of bow waves at different flow velocity conditions are presented in Fig. 13. It can be observed that as the flow

TABLE VI. Resistance forces and wave heights at different flooding angles.

θ ($^\circ$)	F_x (N)	h_1 (mm)	h_2 (mm)	h_{2rms}
15	29.297	58.373	29.779	11.035
22.5	63.913	87.977	30.312	19.889
30	120.452	127.138	132.183	17.085

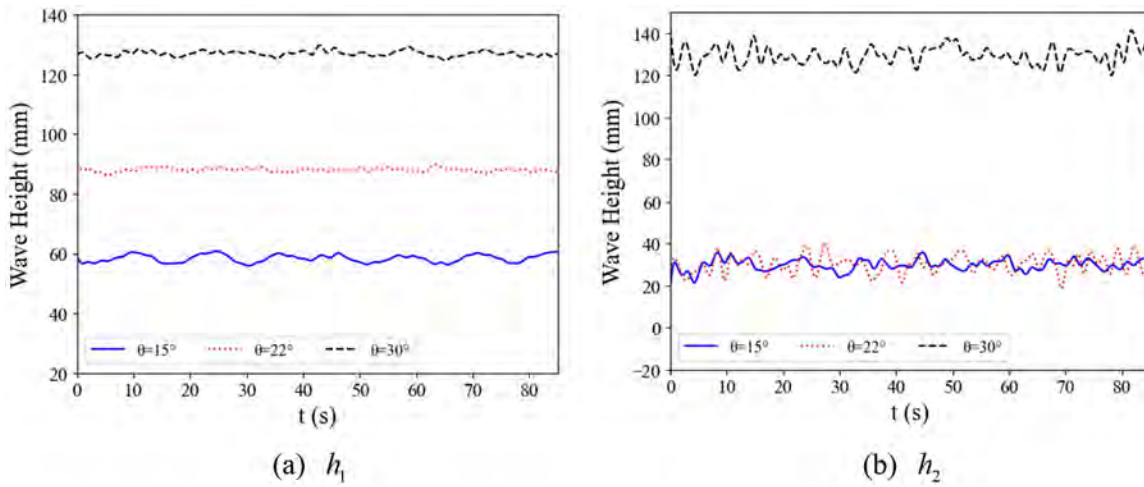


FIG. 10. Time histories of wave height at different flooding angles.

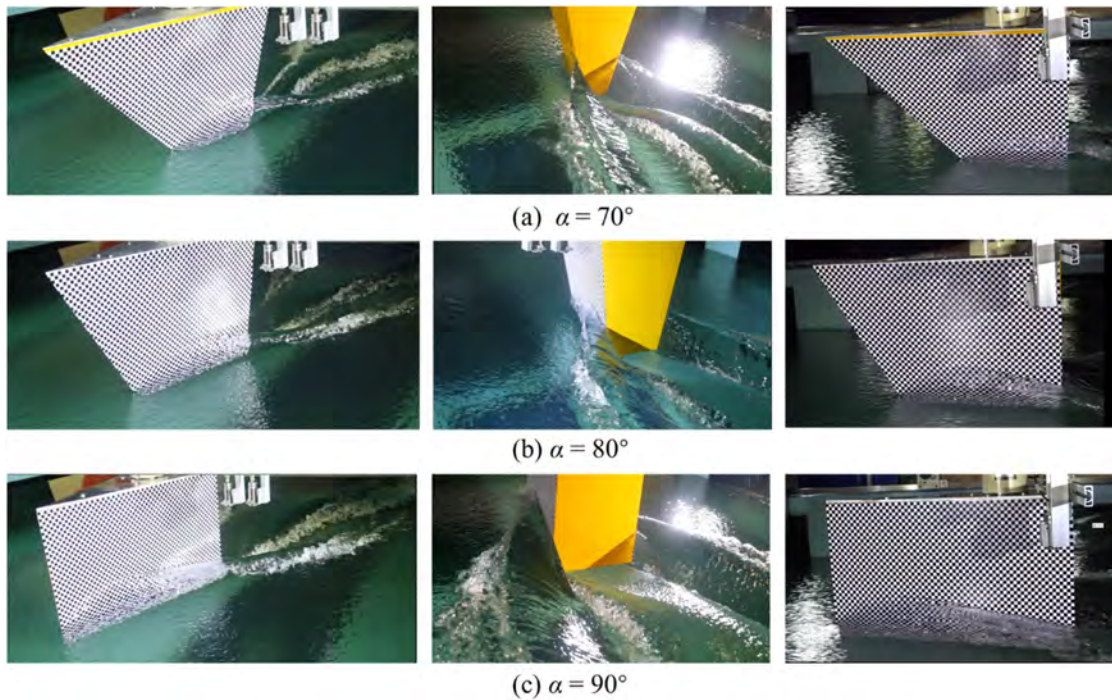


FIG. 11. Experimental images of bow waves at different flare angles.

TABLE VII. Resistance forces and wave heights at different flare angles.

α ($^\circ$)	F_x (N)	h_1 (mm)	h_2 (mm)	h_{2rms}
70	11.157	4.709	3.441	0.927
80	16.636	8.873	3.843	0.918
90	29.297	58.373	29.779	11.035

velocity increases, the wave climbing height along the wedge surface rises, wave breaking becomes more intense, and the transverse extent of the breaking region expands significantly. In the high-velocity case, the scars caused by the plunging wave are more obvious. Additionally, the second wave overturning can be noticed, and the air entrainment becomes increasingly evident with higher flow velocities. These observations align with findings from previous research on ship bow breaking waves.¹⁷

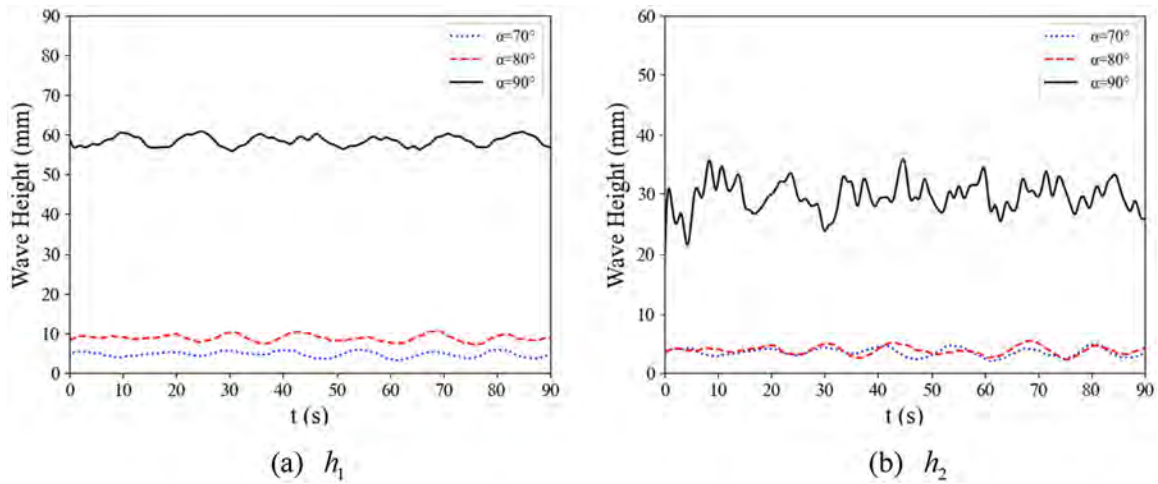


FIG. 12. Time histories of wave height at different flare angles.

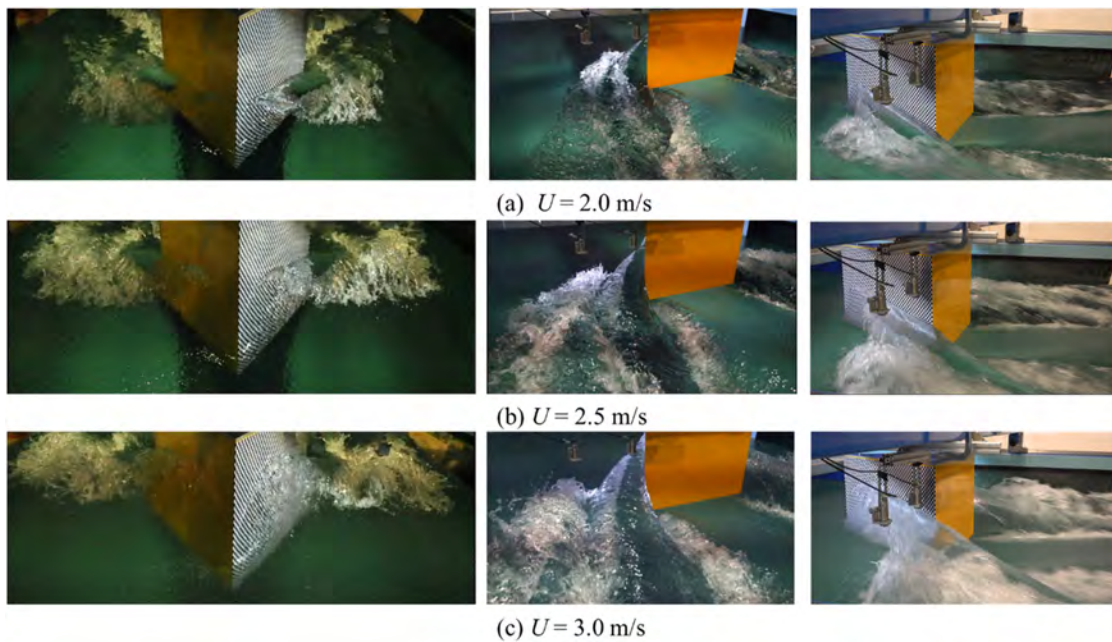


FIG. 13. Experimental images of bow waves at different flow velocities.

Table VIII provides the resistance force and wave height data at the measurement points. Figure 14 presents the time histories of wave height at two locations. With increasing flow velocity, the resistance force acting on the wedge also increases. This is accompanied by higher wave elevation near the wedge surface, leading to a consistent increase in wave height at the h_1 probe, which is positioned closer to the wedge. However, for the h_2 probe, the wave height at $U = 0.30$ m/s is lower than that at $U = 0.25$ m/s. This discrepancy can be

TABLE VIII. Resistance forces and wave heights at different flow velocities.

U (m/s)	F_x (N)	h_1 (mm)	h_2 (mm)	h_{2rms}
2.0	82.675	55.506	47.300	3.848
2.5	120.452	127.138	132.183	11.035
3.0	191.661	167.219	106.415	11.509

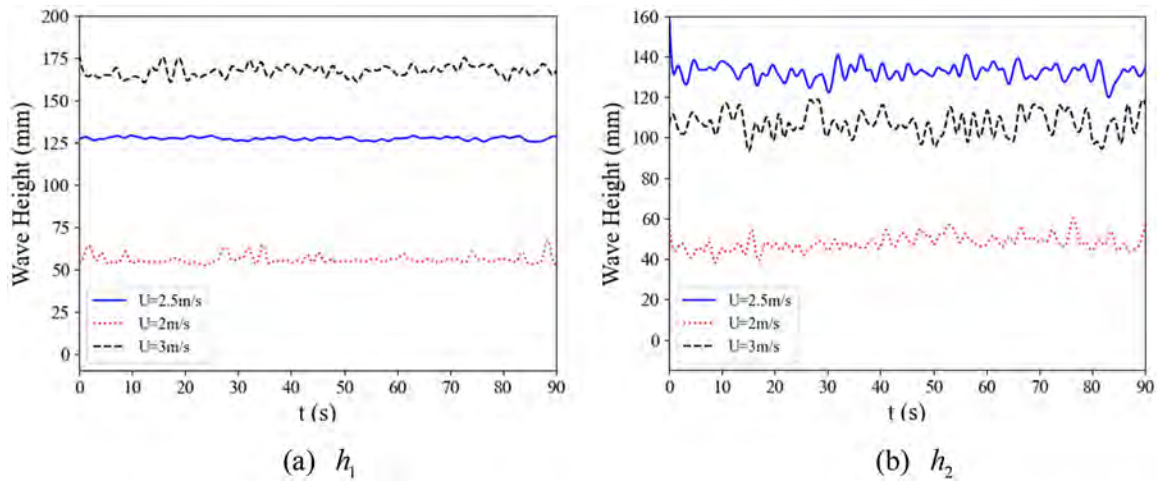


FIG. 14. Time histories of wave height at different flow velocities.

explained by examining Fig. 13. Although higher flow velocities expand the transverse extent of the wave-breaking region, the overall wave overturning area shifts downstream. As a result, the wave height at the h_2 probe, which is farther from the wedge, decreases despite the increased flow velocity. The RMS value is notably smaller in the low-velocity case, which further illustrates that the oscillations of the breaking waves diminish as the velocity decreases.

F. Yaw angle effect

In practical scenarios, a ship’s bow is often not aligned directly with the incoming flow. In this section, different yaw angle conditions are conducted on a wedge-shaped body under a 15° flooding angle and a 90° flare angle. The yaw rotation is defined about the $+Z$ axis, with clockwise rotation considered as a positive yaw angle. The

incoming flow velocity is fixed at 2.5 m/s , and the draft is set to 0.075 m . The wave probe is set at $\Delta Y_1 = 103\text{ mm}$, $\Delta Y_2 = 205\text{ mm}$, and the corresponding wave height is h_1, h_2 .

Figure 15 presents the side view of the wedge bow waves at various yaw angles. In general, as the yaw angle increases, the wave-breaking phenomenon intensifies. Figure 16 shows the time histories of the wave heights. Similar to the observations in Sec. III E, the resistance force on the wedge increases with the yaw angle, and the wave height at measurement point h_1 , located in the non-breaking region, also increases. However, the wave height at h_2 , positioned in the breaking region, shows significant high-frequency fluctuations in the time-history curve.

Table IX lists the measured data of the resistance forces and wave height data at the measurement points. It can be observed that the RMS value in the non-breaking region is relatively small, while the

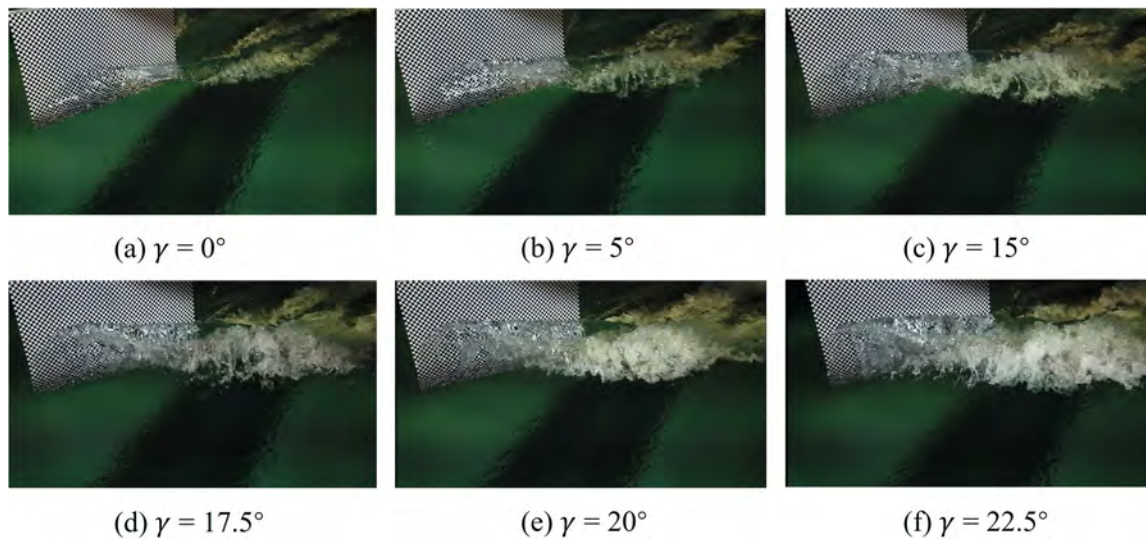


FIG. 15. Experimental images of bow waves at different yaw angles.

29 January 2025 15:21:08

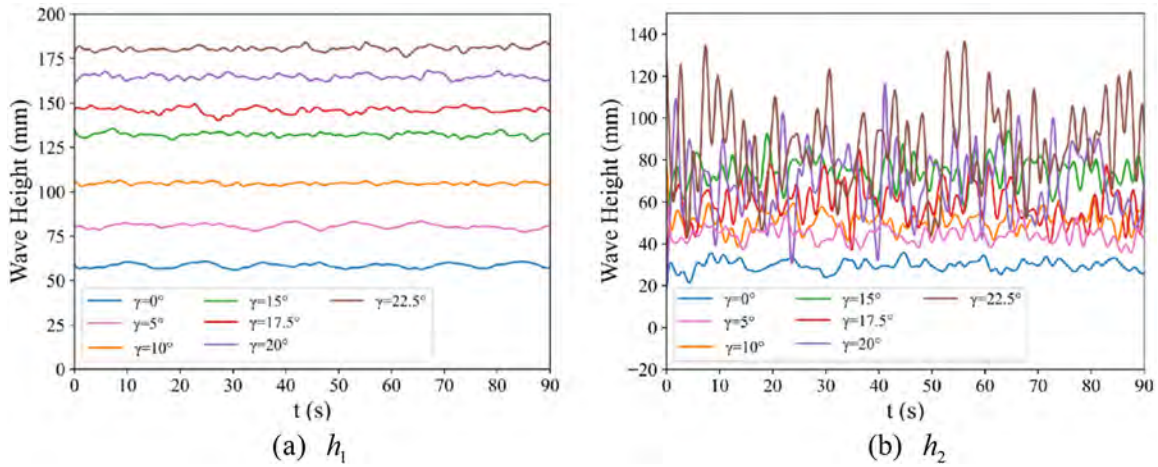


FIG. 16. Time histories of wave height at different yaw angles.

RMS value in the breaking area is significantly larger. Therefore, the RMS value serves as a useful criterion for assessing wave-breaking performance. As the yaw angle increases, the RMS value exhibits a significant increase. Specifically, the RMS value is approximately five times larger in the case of $\gamma = 22.5^\circ$ compared to the case of $\gamma = 0^\circ$. These findings can be used to explain the flow characteristics shown in Figs. 15 and 16.

Figure 17 displays images of wave patterns on the wedge surface captured by a high-speed camera under different yaw conditions. The left-side view indicates that as the yaw angle increases, the wave climbs higher on the wedge surface, with an expanding wave overturning area. In contrast, the right-side view reveals that for yaw angles within $0^\circ \leq \gamma \leq 15^\circ$, the wave height on the right-side surface of the wedge decreases with increasing yaw angles. This is attributed to the right-side plane gradually aligning with the incoming flow direction. However, for $\gamma = 20^\circ$ and $\gamma = 22.5^\circ$, two distinct wave patterns are observed on the wedge surface. One arises from the cutting of the incoming flow at the intersection of the wedge's leading edge and the free surface, forming a jet that moves away from the wedge. The other is generated near the bottom edge of the leading edge, where the high-speed incoming flow overturns, producing a wave closely attached to the wedge surface.

TABLE IX. Resistance forces and wave heights at different yaw angles.

γ ($^\circ$)	F_x (N)	h_1		h_2	
		h_{mean} (mm)	h_{rms}	h_{mean} (mm)	h_{rms}
0°	29.297	58.298	1.732	29.686	11.035
5°	30.507	80.550	1.956	44.212	21.484
10°	33.485	104.778	1.742	51.011	27.921
15°	38.910	132.208	2.249	72.935	38.722
17.5°	43.058	146.099	2.534	58.808	42.264
20°	46.534	165.182	2.744	67.473	50.180
22.5°	50.595	180.621	2.987	90.957	53.318

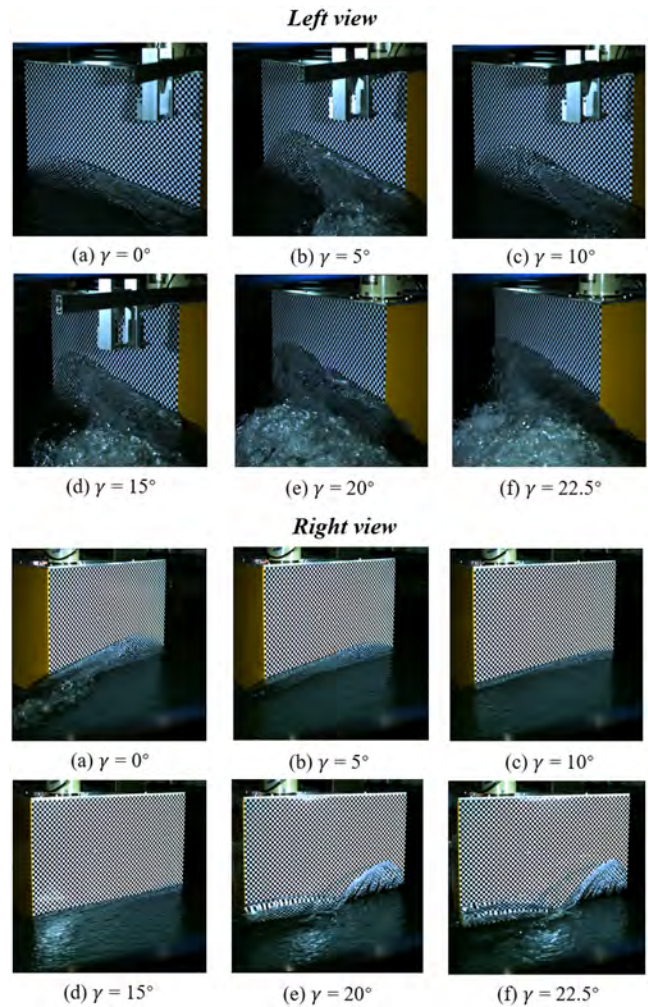


FIG. 17. Experimental images of bow waves with different side views.

29 January 2025 15:21:08

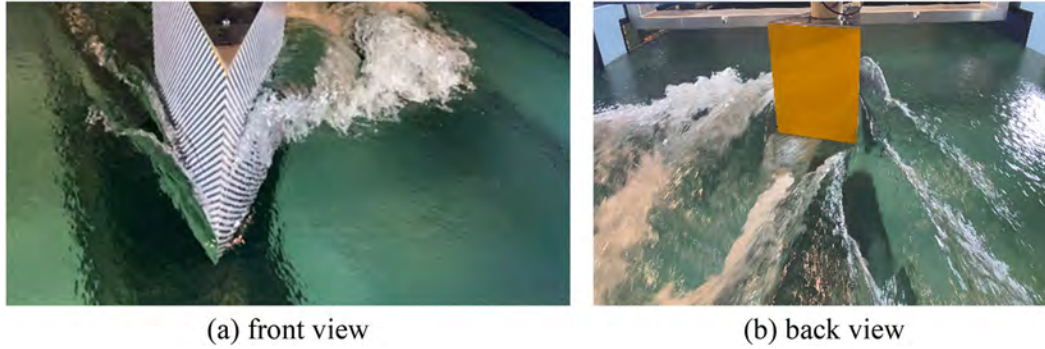


FIG. 18. Experimental images of bow waves at $\gamma = 22.5^\circ$.

Figure 18 shows the front and back views of the wedge under the $\gamma = 22.5^\circ$ condition. The front view reveals two distinct breaking wave overturns on the left side of the wedge and two jet-induced wave patterns on the right side. In the back view, the white foam formed by wave breaking is clearly visible. Compared to the narrower wake of the trailing edge, the bow wave breaking produces a broader region of water-air-bubble mixture flow.

G. Influence of different factors

To better analyze the impact of different factors on resistance and wave height in the wave breaking around wedge-shaped bow, the baseline conditions are set as follows: a velocity of 2.5 m/s, a flooding angle of 15° , a flare angle of 90° , a yaw angle of 0° , and a draft of 0.075 m. The effects of each factor relative to the baseline conditions on resistance, stable wave height (non-breaking region), and unstable wave height (breaking region) are presented in Tables X–XII. The effects on resistance and stable wave height are expressed as average values, while the effects on unstable wave height are described by the RMS value. This approach allows for a normalized investigation of the quantitative effects of different factors on the wave-breaking phenomenon.

Figures 19–21 illustrate the effects of different factors on resistance, stable wave height (non-breaking region), and unstable wave height (breaking region), respectively. It can be observed that the flooding angle has a significant impact on resistance, which helps explain why slender hull designs are commonly used for fast ships. The yaw angle plays a crucial role in affecting the bow waves,

TABLE X. The influence of different factors on resistance.

	Value	2 m/s	2.5 m/s	3 m/s				
U	Deviation	−23.7%	0.00%	50.7%				
	Value	0.05 m	0.075 m	0.1 m				
d	Deviation	−41.9%	0.00%	43.1%				
	Value	15°	22.5°	30°				
θ	Deviation	0.00%	117.4%	308.3%				
	Value	70°	80°	90°				
α	Deviation	−62.06%	−43.42%	0.00%				
	Value	0°	5°	10°	15°	17.5°	20°	22.5°
γ	Deviation	0.00%	3.75%	13.88%	32.33%	46.44%	58.26%	72.07%

TABLE XI. The influence of different factors on wave heights in the stable region.

	Value	2 m/s	2.5 m/s	3 m/s				
U	Deviation	−47.4%	0.0%	63.7%				
	Value	0.05 m	0.075 m	0.1 m				
d	Deviation	−15.6%	0.0%	16.6%				
	Value	15°	22.5°	30°				
θ	Deviation	0.0%	50.7%	117.0%				
	Value	70°	80°	90°				
α	Deviation	−91.9%	−84.8%	0.0%				
	Value	0°	5°	10°	15°	17.5°	20°	22.5°
γ	Deviation	0.0%	38.0%	79.5%	126.5%	150.3%	183.0%	209.4%

influencing both stable wave height and nonlinear breaking waves. These figures provide a clear depiction of how these factors influence resistance and wave breaking.

IV. CONCLUSIONS

This study simplifies the ship’s bow as a wedge-shaped structure and experimentally investigates the bow wave-breaking phenomenon. The aim is to explore various influencing factors and further explain the complex mechanisms behind bow wave breaking. We examine factors such as flow velocity, draft, flooding angle, flare angle, and yaw angle and find that conditions with more intense wave breaking

TABLE XII. The influence of different factors on wave heights in the breaking region.

	Value	2 m/s	2.5 m/s	3 m/s				
U	Deviation	−65.1%	0.0%	4.3%				
	Value	0.05 m	0.075 m	0.1 m				
d	Deviation	−44.5%	0.0%	34.6%				
	Value	15°	22.5°	30°				
θ	Deviation	0.0%	80.2%	54.8%				
	Value	70°	80°	90°				
α	Deviation	−91.6%	−91.7%	0.0%				
	Value	0°	5°	10°	15°	17.5°	20°	22.5°
γ	Deviation	0.00%	94.7%	153.0%	250.9%	283.0%	354.7%	383.2%

29 January 2025 15:21:08

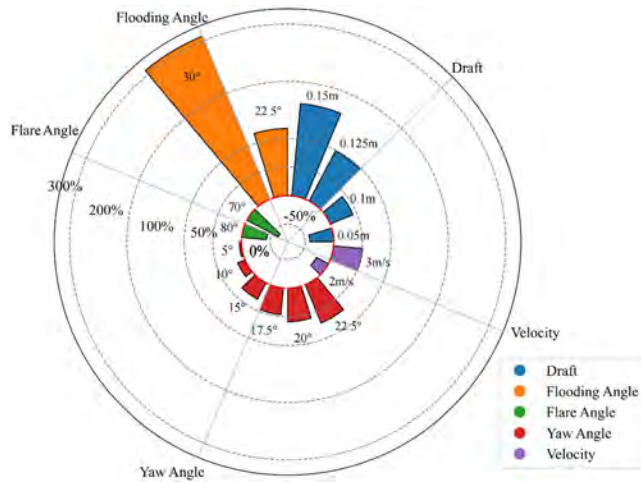


FIG. 19. The influence of different factors on resistance.

typically increase the resistance force on the wedge. In regions close to the structure, where wave breaking does not occur, the wave height can be used with mean value. However, in regions farther from the structure, wave height variation shows significant high-frequency behavior due to the small-scale flow features of wave breaking, and the RMS value must be used to explain the nonlinear phenomena.

The effect of draft primarily influences the increase in resistance due to the growth of the wetted surface area. The characteristics of breaking waves follow a similar trend, with wave height increasing as the wedge draft increases. The influence of resistance and wave height can be up to 43.1% and 44.5%, respectively.

The influence of the flooding angle is significantly greater than that of the draft. A larger flooding angle notably increases both the extent and intensity of wave breaking. This is due to the enhanced blockage effect of the inflow, which promotes higher wave run-up and more intense plunging waves. With an increase in the flooding angle, wave height at the same location can increase dramatically, reaching up to 117%.

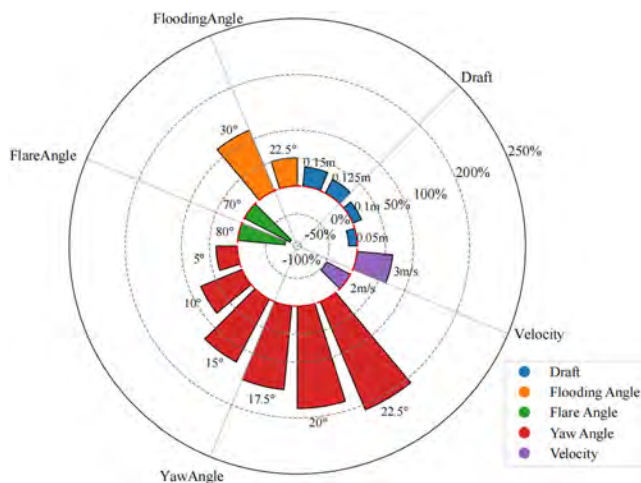


FIG. 20. The influence of different factors on mean wave height in the stable region.

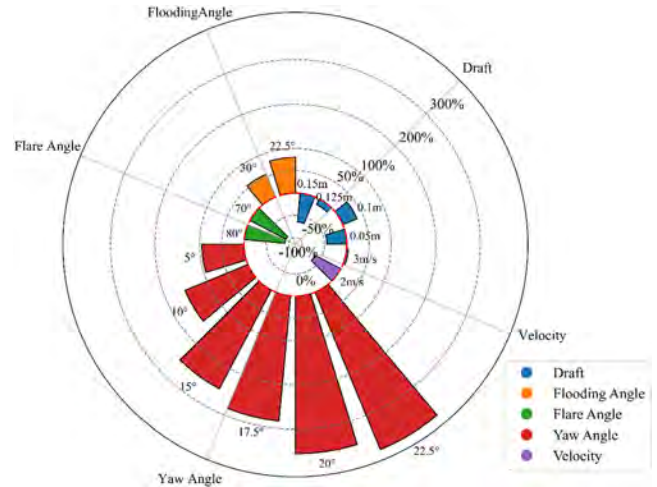


FIG. 21. The influence of different factors on RMS of wave height in the breaking region.

For wave breaking under different flare angle conditions, smaller flare angles result in lower bow wave heights and a more confined wave-breaking and overturning region. Consequently, the resistance force decreases by up to 62.1%. Given the small draft and relatively limited wetted surface area, the reduction in resistance is primarily due to a decrease in wave-making resistance. This observation provides insight into why high-speed vessels often feature flared bow designs.

For the wave breaking under different yaw angle conditions, the wave-breaking phenomenon shows strong asymmetry. For larger yaw angles, more violent plunging wave breaking occurs on the windward side, while no wave breaking is observed on the leeward side for smaller yaw angles. Interestingly, larger yaw angles lead to the formation of two distinct types of jet-induced waves on the leeward side of the wedge. These waves are generated by the interaction between the incoming flow and the bottom corner of the wedge's leading edge as well as the point where the leading edge meets the free surface. The maximum increase in mean value at stable wave region and RMS value at breaking region can be up to 209.4% and 383.2%, respectively.

In the future work, high-fidelity numerical simulations will be employed to further investigate the bow wave-breaking phenomenon. This study will focus on both macroscopic aspects, such as the evolution of the free surface, wave height spectra, and the statistical properties of the breaking region as well as microscopic aspects, including droplet splashing, air entrainment, and bubble sweep-down.

ACKNOWLEDGMENTS

This work was supported by the National Natural Science Foundation of China (Grant Nos. 52471335 and 52131102), to which the authors are most grateful.

AUTHOR DECLARATIONS

Conflict of Interest

The authors have no conflicts to disclose.

Author Contributions

Jianhua Wang: Conceptualization (equal); Data curation (equal); Formal analysis (equal); Investigation (equal); Methodology (equal); Software (equal); Validation (equal); Visualization (equal); Writing – original draft (equal). **Yuming Shao:** Data curation (equal); Formal analysis (equal); Investigation (equal); Visualization (equal). **Xinyi Li:** Data curation (equal); Formal analysis (equal); Investigation (equal); Validation (equal); Visualization (equal). **Tianyi Mao:** Data curation (equal); Formal analysis (equal); Investigation (equal); Validation (equal); Visualization (equal). **Decheng Wan:** Conceptualization (equal); Funding acquisition (equal); Investigation (equal); Project administration (equal); Supervision (equal); Writing – review & editing (equal).

DATA AVAILABILITY

The data that support the findings of this study are available from the corresponding author upon reasonable request.

REFERENCES

- ¹Z. Li, X. Zhang, and D. Wan, “Research progress on the hydrodynamic performance of water-air-bubble mixed flows around a ship,” *J. Hydrodyn.* **34**(2), 171–188 (2022).
- ²X. Zhang, K. He, and D. Wan, “Research progress on mechanism and numerical simulation methods of water-air-bubble mixed flow around marine structure,” *Chin. J. Ship Res.* **17**(3), 1–28 (2022).
- ³L. Deike, “Mass transfer at the ocean–atmosphere interface: The role of wave breaking, droplets, and bubbles,” *Annu. Rev. Fluid Mech.* **54**(1), 191–224 (2022).
- ⁴R. R. Dong, J. Katz, and T. T. Huang, “On the structure of bow waves on a ship model[J],” *J. Fluid Mech.* **346**, 77–115 (1997).
- ⁵G. I. Roth, D. T. Mascenik, and J. Katz, “Measurements of the flow structure and turbulence within a ship bow wave,” *Phys. Fluids* **11**(11), 3512–3523 (1999).
- ⁶J. Longo and F. Stern, “Effects of drift angle on model ship flow,” *Exp. Fluids* **32**(5), 558–569 (2002).
- ⁷A. Olivieri, F. Pistani, R. Wilson *et al.*, “Scars and vortices induced by ship bow and shoulder wave breaking,” *J. Fluids Eng.* **129**(11), 1445–1459 (2007).
- ⁸A. Olivieri, F. Pistani, and A. D. Mascio, “Breaking wave at the bow of a fast displacement ship model,” *J. Mar. Sci. Technol.* **8**(2), 68–75 (2003).
- ⁹D. A. Drazen, A. M. Fullerton, T. C. Fu *et al.*, “A comparison of model-scale experimental measurements and computational predictions for a large transom-stern wave,” 28th Symposium on Naval Hydrodynamics, Pasadena, CA, USA (2014).
- ¹⁰B. Choi, P. R. Wellens, and R. H. M. Huijsmans, “Experimental assessment of effects of bow-wave breaking on added resistance for the fast ship,” *ISP.* **66**(2), 111–143 (2019).
- ¹¹W. Liu, W. Wang, G. Qiu *et al.*, “KCS Unsteady bow wave breaking experiments for physics and CFD validation,” 34th Symposium on Naval Hydrodynamics (SNH), Washington DC, USA (2022).
- ¹²Z. Li, C. Liu, D. Wan *et al.*, “High-fidelity simulation of a hydraulic jump around a surface-piercing hydrofoil,” *Phys. Fluids* **33**, 123304 (2021).
- ¹³Y. Hu, C. Liu, M. Zhao *et al.*, “High-fidelity simulation of an aerated cavity around a surface-piercing rectangular plate,” *Phys. Rev. Fluids* **8**(4), 44003 (2023).
- ¹⁴Y. Shao, W. Wang, D. Wan *et al.*, “Numerical investigations of breaking waves and air entrainment induced by a shallowly submerged hydrofoil,” *Ocean Eng.* **312**, 119026 (2024).
- ¹⁵K. Hendrickson and D. K. P. Yue, “Structures and mechanisms of air-entraining quasi-steady breaking ship waves,” *J. Ship Res.* **63**(02), 69–77 (2019).
- ¹⁶K. Hendrickson, G. D. Weymouth, X. Yu *et al.*, “Wake behind a three-dimensional dry transom stern. Part 1. Flow structure and large-scale air entrainment,” *J. Fluid Mech.* **875**, 854–883 (2019).
- ¹⁷J. Wang, Z. Ren, and D. Wan, “Study of a container ship with breaking waves at high Froude number using URANS and DDES methods,” *J. Ship Res.* **64**(4), 346–356 (2020).
- ¹⁸J. Wang, W. Zhao, and D. Wan, “Development of nano-FOAM-SJTU solver based on OpenFOAM for marine hydrodynamics,” *J. Hydrodyn.* **31**, 1–20 (2019).
- ¹⁹D. Wu, J. Wang, and D. Wan, “Delayed detached eddy simulation method for breaking bow waves of a surface combatant model with different trim angle,” *Ocean Eng.* **242**, 110177 (2021).
- ²⁰W. H. R. Chan, P. L. Johnson, P. Moin, and J. Urzay, “The turbulent bubble break-up cascade. Part 2. Numerical simulations of breaking waves,” *J. Fluid Mech.* **912**, A43 (2021).
- ²¹W. Mostert, S. Popinet, and L. Deike, “High-resolution direct simulation of deep water breaking waves: Transition to turbulence, bubbles and droplets production,” *J. Fluid Mech.* **942**, A27 (2022).
- ²²J. R. King, S. J. Lind, B. D. Rogers, P. K. Stansby, and R. Vacondio, “Large eddy simulations of bubbly flows and breaking waves with smoothed particle hydrodynamics,” *J. Fluid Mech.* **972**, A24 (2023).
- ²³T. A. Waniewski, C. E. Brennen, and F. Raichlen, “Bow wave dynamics,” *J. Ship Res.* **46**(01), 1–15 (2002).
- ²⁴T. A. Waniewski, *Air Entrainment by Bow Waves* (California Institute of Technology, 1999).
- ²⁵T. A. Waniewski, C. E. Brennen, and F. Raichlen, “Measurements of air entrainment by bow waves[J],” *J. Fluids Eng.* **123**(1), 57–63 (2001).
- ²⁶A. Karion, T. C. Fu, T. W. Sur *et al.*, *Experiment to Examine the Effect of Scale on a Breaking Bow Wave* (Hydromechanics Department, Naval Surface Warfare Center, Carderock Division, 2004).
- ²⁷F. Noblesse, G. E. R. Delhommeau, M. Guilbaud *et al.*, “Simple analytical relations for ship bow waves,” *J. Fluid Mech.* **600**, 105–132 (2008).
- ²⁸G. Zhu, Y. Feng, Z. Chen, and H. Lu, “Hydrodynamic design of a circulating water channel based on a fractional-step multi-objective optimization,” *Ocean Eng.* **251**, 110959 (2022).